Application of a nested-grid ocean circulation model to a shallow coastal embayment: Verification against observations

Li Zhai, Jinyu Sheng and Richard J. Greatbatch
Department of Oceanography, Dalhousie University, Halifax, NS, Canada, B3H 4J1

Short title: APPLICATION OF A COASTAL CIRCULATION MODEL

SUBMITTED TO *JOURNAL OF GEOPHYSICAL RESEARCH ON MARCH 19, 2007*

Abstract.

A nested-grid ocean circulation modelling system is used to study the response of Lunenburg Bay in Nova Scotia, Canada, to local wind forcing, tides, remotely generated waves, and buoyancy forcing in the summer and fall of 2003. Quantitative comparisons between observations and model results demonstrate that the modelling system reproduces reasonably well the observed sea level, temperature, salinity, and currents in the bay. Numerical results reveal that the spatial and temporal variability of temperature and salinity in the bay during the study period is mainly forced by the local wind stress and surface heat/freshwater fluxes, with some contribution from tidal circulation. In particular, the local heat balance on the monthly time scale is dominated by cooling due to vertical advection and warming due to horizontal advection and net surface heat flux, while high-frequency variations (time scales of 1$\sim$30 days) are mainly associated with vertical advection, i.e. wind-induced upwelling and downwelling. There is also a strong baroclinic throughflow over the deep water region outside Lunenburg Bay that is strongly influenced by wind forcing. The vertically-integrated momentum balance indicates a modified geostrophic balance on the monthly time scale and longer, and is dominated by the pressure term and wind minus bottom stress in the high-frequency band, consistent with barotropic dynamics.

1. Introduction

Waters on the continental shelf and in adjacent semi-enclosed seas, referred to as coastal waters [*Bowden*, 1983], account for only 3% of all the sea surface area and 0.5% of total ocean volume, but are very important in terms of ocean habitats and resources. Most of the world's major fisheries are in coastal waters and physical conditions in the regions play a significant role in their productivity. Without information on physical processes one cannot determine whether temporal or spatial variations in biomass density are due to chemical or biological activity or simply due to water mass movement.

Upwelling has been observed in many coastal regions and lakes [*Csanady*, 1974; *Clarke*, 1977; *Crépon et al.*, 1984]. *Hachey* [1935] first reported the phenomenon of coastal upwelling on the Scotian Shelf. *Petrie et al.* [1987] presented a simple dynamical interpretation of coastal upwelling and eddy development off Nova Scotia using a linear two-layer model. Upwelling is not always a local response to the wind, however, because baroclinic Kelvin waves can carry information along the coast [*Gill*, 1982]. In the upwelling region along the Peru coast, for example, sub-tidal sea level variations with periods of days to weeks are a manifestation of poleward propagating internal Kelvin waves [*Brink et al.*, 1978]. *deYoung et al.* [1993] discussed the baroclinic response of Conception Bay, Newfoundland, to wind forcing, and demonstrated the nonlocal effects of internal Kelvin waves using a reduced gravity model. *Davidson et al.* [2001] showed that the asymmetric baroclinic response of Conception Bay to wind forcing is associated with the higher-order baroclinic modes of internal Kelvin waves. While these studies have indicated that baroclinicity affects the circulation and the thermal structure in coastal waters, investigation and quantification of its effects in the region of a shallow coastal embayment remain to be examined.

In this paper, we focus on Lunenburg Bay (hereafter LB) in Nova Scotia, Canada, which is a shallow coastal embayment located on the southern coast of Nova Scotia, with a surface extent of about 8 km by 4 km and a maximum water depth of 25 m. In 2002, a multidisciplinary coastal observatory was established in

LB (http://www.cmep.ca/bay, *Wang et al.*, 2007). The observatory has two major components: a real-time observational component and a coupled modelling component. Here we describe the physical part of the modelling system, compare the model results against the observations to quantify the model performance, and use the ocean circulation model to gain insight into the essential dynamics governing LB on time scales from hours to months.

The barotropic circulation in LB has been studied by a number of authors. *Sturley and Bowen* [1996] used a Galerkin spectral model to study the barotropic tidal jet and tidal asymmetry in LB, and *Thompson et al.* [1998] used the same model to interpret synthetic aperture radar images of the surface circulation in LB. More recently, *Sheng and Wang* [2004] used a z-level coastal circulation model (CANDIE) to study barotropic tides and nonlinear tidal dynamics in LB, and *Wang et al.* [2007] used the same model to simulate the storm-induced circulation in LB during Hurricane Juan of 2003. None of these previous efforts attempted to model the temperature and salinity structure and variability in the bay. *Zhai et al.* [2007] have shown that the observed temperature and salinity in LB had significant spatial and temporal variability in the summer and fall of 2003, and demonstrated the importance of both local (i.e., surface heating) and non-local (i.e. advective) processes based on the analysis of heat budget. The observed non-tidal currents were also found to have significant temporal variation, with the first EOF (empirical orthogonal function) mode correlated with the local wind forcing, and the second EOF mode related to the vertical shear of the horizontal currents estimated from horizontal density gradients based on the thermal wind relation [*Zhai et al.*, 2007]. To further understand the dynamics of LB, the modelling system described here includes temperature and salinity as prognostic variables. Furthermore, the model for LB is nested inside a larger domain model including Mahone Bay, located to the northwest and "upstream" of LB in the sense of Kelvin wave propagation, creating a baroclinic version of the nested-grid coastal circulation modelling system introduced in *Sheng et al.* [2007].

The arrangement of this paper is as follows. Section 2 outlines the nested-grid modelling system. Section 3 presents the simulated circulation and temperature fields during upwelling and downwelling events, and describes three additional numerical experiments designed to illustrate the dynamics. Section 4 assesses model performance based on the comparison of observations and model results. Section 5 examines the heat budget and section 6 examines the vertically-integrated momentum balance. A summary and conclusions are given in section 7.

2 The nested-grid circulation modeling system

2.1 Ocean circulation model and setup

The nested-grid modelling system is based on the free surface version of CANDIE [*Lu et al.*, 2001; *Sheng and Wang*, 2004], which is a primitive equation model formulated in the finite-difference form with a z-level in the vertical. The nested-grid system used in this paper has a fine-resolution inner model embedded in a coarse-resolution outer model (Figure 1). The outer model covers Mahone Bay (MB), Lunenburg Bay (LB) and Rose Bay (RB), with a horizontal resolution of ∼500 m. The inner model covers LB and RB, with a horizontal resolution of ∼200 m. The use of 200 m grid spacing ensures that the first three baroclinic radii of deformation in the bay (3.1 km, 1.4 km and 0.9 km, respectively; see *Zhai et al.*, 2007) are reasonably well resolved in the finer-resolution inner model. Both the inner and outer models have 24 z-levels with a vertical resolution of 1 m, except for 3 m for the top z-level, and 4.5 m below 20 m depth. It should be noted that the outer model does not resolve Upper South Cove (USC) and Lower South Cove (LSC). In comparison, the inner model does resolve the two coves, but poorly resolves the mouth of USC.

The nested-grid modelling system uses the hydrostatic and Boussinesq approximations in the model governing equations, and the 4th order numerics [*Dietrich*, 1997] and a flux limiter [*Thuburn*, 1996] to reduce numerical dispersion of the advection terms in the model. The modified version of the KPP (K-profile parameterization, *Large et al.*,

1994) vertical mixing scheme is used [*Durski et al.*, 2004], together with the horizontal mixing scheme of *Smagorinsky* [1963] for which the Prandtl number (the ratio between eddy diffusivity and viscosity) is set to 0.1 for the inner model. A quadratic bottom stress parameterization is used with a drag coefficient of 3×10^{-3}, apart from in the neighbourhood of USC and LSC where a spatially variable and relatively larger drag coefficient is used (see *Sheng and Wang* [2004] for details).

The nested-grid modelling system is initialized from rest with horizontally uniform, but vertically stratified temperature and salinity. The initial vertical profiles of temperature and salinity in the top 25 m are based on the observations in LB, and below 25 m are based on the hydrographic surveys at station 2 on the inner Scotian Shelf (Figure 1) in the summer of 2003.

2.2 Model forcings at surface

The nested-grid modelling system is forced by the time-varying and spatially uniform wind stress (Figure 2a) and net sea surface heat flux constructed from the observations by *Zhai et al.* [2007]. The total surface heat flux seen by the model is given by

$$Q_{net} = Q^{input} + \beta(SST^o - SST^m), \tag{1}$$

where Q^{input} is the net surface heat flux taken from *Zhai et al.* [2007] (Figure 2c), SST^o is the observed sea surface temperature at MB1, SST^m is the model sea surface temperature, and β is the coupling coefficient defined as $\Delta z_1 \rho_0 c_p/\tau$, where Δz_1 is the thickness of the top z-level, c_p is the specific heat, τ is the restoring time scale set to 10 days. The part of the net surface heat flux associated with downward solar irradiance is distributed as a function of depth and represented by the expression suggested by *Paulson and Simpson* [1977] and given by

$$I = Q_I[Re^{z/\xi_1} + (1-R)e^{z/\xi_2}]; \tag{2}$$

where I is the irradiance at z, $R = 0.62$, ξ_1 and ξ_2 are attenuation lengths equal to 1.5 and 20 m, respectively, and z is the vertical coordinate, positive upward with the origin at mean sea level.

The net surface freshwater flux is diagnosed from the numerical model using the following approach due to the lack of observations. We first integrate the model with the surface freshwater flux set to zero. The transfer function (i.e. difference in magnitude) between the modeled sea surface salinity, SSS_m, and observed sea surface salinity, SSS_o, at MB1 is determined, and then used to estimate the evaporation minus precipitation $E - P = \frac{\Delta z}{SSS_o}\frac{\partial}{\partial t}(SSS_0 - SSS_m)$ to produce the time series shown in Figure 2d.

2.3 Model forcings along open boundaries

Along the outer model open boundaries, the radiation condition of *Davies and Flather* [1978] is used:

$$U_B^n = U_p^n + \frac{c}{h}(\eta_B^n - \eta_t^n - \eta_r^n), \tag{3}$$

where U_B^n and η_B^n are the model-calculated normal flow and surface elevation at the open boundaries, U_p^n is a specified normal flow and set to be U_{B-1}^n for simplicity, c is the phase speed, h is the local water depth, η_t^n is the tidal elevation, and η_r^n represents the remotely generated waves. Superscript n indicates the time step, subscript B represents the boundary grid point, and $B - 1$ is the interior model grid point closest to the open boundary. Time series of η_t shown in Figure 2b is determined using the simplified incremental approach discussed in *Sheng and Wang* [2004] from the tidal sea level prediction at Lunenburg Harbour, which was made by the Canadian Hydrographic Service using more than 60 tidal constituents determined from the historical sea level observations at the harbour. Time series of η_r in Figure 2b is determined from the observed non-tidal sea level at SB2 [*Zhai et al.*, 2007] using the same method.

Adaptive boundary conditions are used for temperature and salinity at the outer model open boundaries. It first uses an explicit *Orlanski* [1976] radiation condition to determine whether the open boundary of the outer model is passive (outward

propagation) or active (inward propagation). If the open boundary is passive, the model temperature and salinity are radiated outward. If the open boundary is active, the model temperature and salinity at the open boundary are restored to the observed temperature and salinity at Station 2 on the inner Scotian Shelf (Figure 1), with a restoring time scale of 10 days. Satellite observations of the sea surface temperature (not shown) suggest that bands of cool water disappeared off Halifax and along the western half of the shore, and the warm inner-shelf water gradually moved towards the coast and extended southwestward from day 250 to 270. Therefore, a shorter restoring time scale of 0.1 day is used at the outer model open boundaries to represent the influence of these observations during this period.

At the inner model open boundaries, the temperature and salinity fields are also updated using the adaptive boundary condition described above, except that they are restored to the temperature and salinity calculated by the outer model and interpolated onto the inner model grid, with the restoring time scale set to 0.1 day. In addition, the normal flow along the open boundaries of the inner model is calculated by (3) with U_p^n, η_t^n and η_r^n taken from the outer model results and interpolated onto the inner model grid.

3. An upwelling-downwelling event in August 2003

Observations suggest that water temperatures with periods of 1∼10 days have strong spatial variability associated with wind-induced upwelling and downwelling [*Zhai et al.*, 2007]. Here, an examination of such events is made using the inner model results when the nested-grid modelling system is driven by the complete suite of forcings, referred to as the "control" run (Exp-Control, Table 1). Three additional model experiments (Table 1) were also conducted to isolate the dynamical influences of wind, tides, and baroclinic effects on the circulation and temperature fields. The nested-grid modelling system is forced by the wind and buoyancy forcing in the first additional experiment (Exp-Wind), and by the tide and buoyancy forcing in the second experiment

(Exp-Tide). In the third experiment referred to as the barotropic run (Exp-Baro), the modelling system is forced by wind only, and temperature and salinity are set to be uniform. Other model parameters are the same as in the control run. All model runs begin on day 224, and here we focus on a period from day 234 to 237 during which temperature and salinity have significant spatial variations.

3.1 Circulation

The near-surface (3.5 m) and sub-surface (7.5 m) currents and temperatures shown in Figures 3a-c and 4a-c are those produced by the inner model in the control run at 0000 UTC August 22 (day 234.0), 1424 August 23 (day 235.6), 1912 August 25 (day 237.8) 2003, respectively. The local wind stress at day 234.0 is northeastward with a magnitude of $\sim$0.1 Pa. The simulated near-surface currents at this time (Figure 3a) are nearly northeastward over the deep water region to the east of LB and RB, and asymmetric inside LB in the sense that the southeastward currents are stronger over northern LB than those over southern LB. The strong ebb tidal jet is evident exiting Corkum's Channel. The simulated sub-surface currents at this time (Figure 4a) are nearly northward outside LB, and are relatively weak inside LB. A comparison of the model-calculated currents from the three additional numerical experiments (Figures 3-4 d, j, g) shows that the coastal currents in the control run are mainly forced by wind, whereas the jet-like flows through Corkum's Channel and over eastern East Point Island are largely generated by the tidal forcing. Baroclinicity also plays an important role in generating the asymmetric currents in LB.

By day 235.6 the wind stress has changed to southeastward with an amplitude of $\sim$0.1 Pa. There is a strong and nearly southward throughflow over the deep water region outside LB at this time in the control run (Figure 3b). The currents inside LB flow southeastward, and veer southward on reaching the deep water region. The currents near southern East Point Island are relatively weak. The sub-surface currents (Figure 4b) are characterized by compensating return flow inside LB and southward

throughflow east of EPI and in the region of deeper water outside LB. A comparison of model-calculated currents from the three additional experiments (Figures 3-4 e, h, k) shows that the throughflow in the control run at this time is strongly affected by the baroclinicity, and that baroclinic effects enhance the subsurface return flow over southern LB. The tidally-forced currents are relatively weak in LB at this time.

The wind stress has relaxed almost completely by day 237.8. At this time, the near-surface currents in the control run (Figure 3c) flow northward over the deep water region, and veer northwestward when entering the bay. There are strong southwestward inflows through Corkum's Channel, indicative of the incoming tide. The sub-surface flow in the control run (Figure 4c) is dominated by the incoming tide, but with weaker inflow on the south side of the bay where the wind forcing-only case shows a southeastward flow out of the bay. In a later study, we shall argue that internal Kelvin waves are generated around East Point Island, propagate into the bay and enhance the northwestward near-surface flow over northern LB.

3.2 Temperature

The temperature fields shown in Figures 3 and 4 demonstrate that the three-dimensional circulation plays a significant role in generating the spatial variability of temperatures in LB, since the surface heat flux used to drive the modelling system in this study is spatially uniform (apart from the relatively weak restoring term in equation (1)). The simulated near-surface (3.5 m) temperatures on day 234.0 in the control run (Figure 3a) are characterized by relatively cold water of about 12°C over the deep water region to the south of LB and east of RB. The colder (warmer) water of less (greater) than 15°C over southern (northern) LB at this time are caused by wind-induced local upwelling (downwelling). The water temperatures are above 15°C in the two coves and southwestern RB due mainly to the shallow topography. The simulated sub-surface (7.5 m) temperatures in the control run at this time (Figure 4a) are relatively cold and below 7°C in RB and over eastern LB associated mainly with local upwelling and

horizontal advection. There is relatively warm water over inner LB associated with the shallow local topography. A comparison of the model-calculated temperatures from the two additional, baroclinic numerical experiments (Figures 3-4 d, g) shows that the spatial pattern of near-surface temperatures is mainly generated by wind forcing, except that the warm temperature front at the mouth of Corkum's Channel is advected northeastward by the strong tidal jet compared to the run with wind forcing only (Exp-Wind). With tidal forcing only (Exp-Tide), the temperature fields are nearly horizontally uniform at the surface (Figure 3g), and have weak horizontal variation at sub-surface depth due to the interaction of topography and the thermocline (Figure 4g).

The simulated near-surface temperature on day 235.6 in the control run (Figure 3b) is characterized by relatively warm water over the deep water region outside LB, due to the southward advection of warm water from MB. The near-surface temperature has a large difference of about 5°C between northern LB and southern LB, associated with local wind-induced upwelling and downwelling. The coastal water in the two coves is relatively warm. The simulated sub-surface temperature in the control run at this time (Figure 4b) is nearly uniform and colder than 7°C inside LB. The sub-surface temperature is relatively warm at the entrance of LB due to the advection of warm water from southern MB. A comparison of model-calculated temperatures from the additional numerical experiments (Figures 3-4 e, h) shows that the spatial pattern of temperature in the control run is similar to that forced by wind only (Exp-Wind). However, without tidal forcing, the temperatures forced by wind alone tend to be warmer than those in the control run.

By day 237.8, the simulated near-surface temperature in the control run (Figure 3c) is warmer over the deep water region outside LB than in Figure 3b. At this time, warm water is being advected northward into the region. The near-surface temperature inside LB has weak spatial variation, but with relatively warm water being advected into the bay by the northwestward flow, especially on the northern side of the bay. The cold temperature front is being advected southwestward through Corkum's Channel

into two coves by the incoming tide. The sub-surface temperature is nearly uniform and about 10°C over the study region. A comparison of model-calculated temperatures from the two baroclinic experiments shown in Figures 3-4 f, i shows that the spatial pattern of temperatures in the control run is generated by the wind and tidal forcing. In the absence of tidal advection and mixing, the temperatures forced by wind only (Figures Figures 3g-i) tend to be warmer than those in the control run. Temperatures forced by tides only (Figures 3d-f) are patchy implying the interaction of flood tidal currents and topography.

4 Assessing the model performance

The hindcast skill of the nested-grid modelling system is examined by comparing the inner model results in the control run with the observations made in LB during the study period. The model hindcast skill is quantified in terms of the γ^2 values defined as [*Thompson and Sheng*, 1997]:

$$\gamma^2 = \frac{Var(O - M)}{Var(O)}, \tag{4}$$

where O and M are the observed and model-calculated variables respectively, and Var is the variance, and all variables are sampled every half an hour. The γ^2 value is a measure of the variance of the hindcast error upon the variance of the observations. The smaller γ^2 is, the better the model results fit the observations. It should be noted that γ^2 could be greater than unity. In the case of $\gamma^2 > 1$, the variance of the observations increases with the subtraction of the model results from the observations.

4.1 Surface elevation

To examine the model performance in simulating surface elevations in LB, the tidal and non-tidal components of simulated and observed sea levels at five locations in the bay are decomposed using the tidal analysis package developed by *Pawlowicz et al.* [2002]. The comparison of the three major constituents of semi-diurnal tidal

elevations (M_2, N_2, and S_2) is shown in Table 2 and Figure 5. The differences between the simulated and observed amplitudes of the three major constituents are generally less than 1 cm. The differences in phases are generally less than 15° (0.5 hour). The good agreement of the simulated and observed tidal elevations indicates that the inner model generally performs well in simulating the tidal elevations. In addition, the inner model reproduces the significant reduction of semi-diurnal tidal elevations in USC, which is mainly associated with the hydraulic control and nonlinear tidal dynamics as discussed in *Sheng and Wang* [2004].

The observed and simulated non-tidal sea levels are shown in Figure 6 (by "non-tidal" we mean the sea level with the tides removed). The time series in this figure demonstrate that the inner model in the control run also captures very well the rapid changes in the non-tidal sea level associated with Hurricane Juan on September 29, 2003 (day 271), the major event in the time series. The γ^2 values are about 0.1 in LB and about 0.4 in USC, indicating that the inner model generally performs better in simulating non-tidal sea levels in LB than in USC, which is due to the poor representation of the narrow mouth of USC.

4.2 Temperature and salinity

Figures 7 and 8 demonstrate that the inner model in the control run performs reasonably well in reconstructing the observed temperature and salinity at the three sites SB2, SB3 and MB1 in LB. The inner model generally reproduces the month-to-month variability of the observed temperature and salinity in the bay. In addition, the inner model also captures several upwelling-downwelling events and reproduces the spatial variations of temperatures and salinities at the three sites. However the inner model tends to generate larger high-frequency variability (< 10 days) in the sub-surface temperature and salinity at the three sites between day 272 and 280. The γ^2 values are typically less than 0.25 for temperature, and generally less than 0.4 for salinity. Note that the large γ^2 value of 0.53 at 6-m depth at SB2 for salinity may be due to problems

with the instrument around day 299.

To further examine the model skill in simulating the vertical structure of temperatures at site SB3, the time-depth distribution of simulated temperatures in the control run are compared with the observed temperature made by minilog temperature recorders and pressure-temperature sensors at site SB3 (Figure 9). The inner model captures the dominant features of the evolving thermal stratification. The water column at the site is strongly stratified in August (day 213 to 243), becomes weakly stratified in September (day 244-273), and restratifies again in October (day 274-304). There are strong isotherm displacements with periods of several days during the first 25 days. The 7°C isotherm rises by about 7 m, then returns to its original depth over several days, as a consequence of wind-induced upwelling and downwelling. In the middle of the record, there is a strong downward displacement of the 14°C isotherm. This is followed by a fairly steady rise of the temperature throughout the water column until day 280. As described in section 5, this is due to a combination of net surface heat input and advection of warm water into the bay. On 29 September (day 271), the temperature of the whole water column reaches 18°C and is well-mixed in association with the strong vertical mixing induced by Hurricane Juan. Before the end of the record, the 7°C isotherm reappears due to local upwelling and advection of cold water into the bay.

Figure 9c shows the difference, observed minus simulated temperatures at SB3. There are warm biases of $\sim$2°C from day 240-250 and cold biases of $\sim$5°C below 5 m depth from day 272-280 after Hurricane Juan in the model temperatures. Both of which seem likely to be associated with the model open boundary conditions. The γ^2 values, also shown in the figure, are less than 0.3, but have a tendency to increase with depth, probably due to the specification of temperature along the model open boundaries. Further improvement of the open boundary conditions can be done by using a three-level nesting or data assimilation technique, but is not pursued further in this study.

4.3 Currents

We next assess the model hindcast skill in simulating the three-dimensional circulation in LB. Figure 10 shows the time series of observed and simulated currents at SB3 and SB2 from day 234 to 244 when there are relatively large baroclinic effects as shown in Figures 3 and 4. The inner model in the control run captures the general features of the circulation, that is both the semi-diurnal tidal currents and the non-tidal currents. From day 234-236, when the wind stress is roughly northward, the simulated sub-surface non-tidal currents at SB3 are characterized by northwestward inflow of $\sim$5 cm s^{-1} (see also Figure 4). From day 236-238 when the wind stress is roughly eastward, there is approximately eastward non-tidal outflow of $\sim$5 cm s^{-1} at SB3, and from day 238-240 when the wind dies down, the non-tidal currents are characterized by weak northwestward return flow at SB3. The γ^2 values typically range from 0.4 to 0.8 for the eastward component, and from 0.9 to 1.3 for the northward component. Generally speaking, the model does better just below the surface and with along-bay rather than cross-bay currents.

Tidal analyses of the observed and simulated currents (Table 3 and Figure 11) indicate that the M_2 tidal flow explains more than 50% of the total variance of tidal currents at sites SB2, SB3 and MB1, which is consistent with the previous findings of *Sheng and Wang* [2004]. The inner model reproduces reasonably well the characteristics of the observed M_2 tidal current ellipses. Note that the semi-minor axes have large analysis error since the signal-to-noise ratio (defined as the square of the ratio of amplitude to amplitude error) is smaller than one. The M_2 tidal currents are nearly rectilinear and aligned roughly with the bottom topography at sites SB3 and MB1, but have relatively large ellipticity at SB2 due mainly to the influence of the jet-like flow through Corkum's Channel. The semi-major axes of M_2 tidal current ellipses reduce near the bottom at sites SB2 and MB1, due likely to bottom friction. There is generally good agreement between the simulated and observed semi-major axes at the three sites, but relatively large errors at 10.5-m depth at SB3 and MB1, probably due to the less

accurate representation of the topography. The simulated orientations and phases of M_2 tidal current ellipses agree reasonably well with the observed ones at the three sites with errors typically less than 10°.

To examine the model performance in simulating the horizontal structure of the currents at sub-tidal frequencies, the currents are low-pass filtered with a cutoff period of 27 hours. Means and variances of the simulated sub-tidal currents are calculated at the three sites from day 260 to 293, and compared with observations (Figure 12). The simulated mean current at 4.5 m is nearly eastward at MB1 and in the same direction as the observations. The simulated mean currents at SB3 and SB2 are aligned with the bottom topography and tend to be larger than in the observations. The major axes of variance of simulated sub-tidal currents at 4.5 m are in the same direction as those of the observations, but have smaller magnitudes, indicating that the nested-grid system generates smaller variability. Principal component analysis [*Emery and Thomson*, 1998] demonstrates that the first mode of the simulated and observed sub-tidal currents accounts for 43% and 47% of the variance respectively and shows similar spatial patterns (Figure 13). The eigenvector for the first mode shows oppositely directed currents at MB1 and SB3, indicating that circulation around the bay in both the model and the observations. The time series of the first mode coefficient from the simulation has a smaller amplitude, especially during large wind events, than that from the observations, again suggesting that the nested-grid system underestimates the observed sub-tidal currents at sites SB2 and MB1.

5. Heat and salt budgets

One of the important features for the hydrography in coastal waters is the relative role of the local and nonlocal processes in determining the heat budget. LB is no exception. Using the observations alone, *Zhai et al.* [2007] found evidence from the observations that advection associated with the first EOF mode shown in Figure 13 played an important role at low frequencies in the heat budget of LB. Using the model

results in the control run, we are better able to quantify the role of advection and horizontal mixing. In this section, the depth-integrated heat budget is examined by using

$$\underbrace{\frac{\partial H}{\partial t}}_{A} = \underbrace{- < u\frac{\partial T}{\partial x} >}_{B} \underbrace{- < v\frac{\partial T}{\partial y} >}_{C} \underbrace{- < w\frac{\partial T}{\partial z} >}_{D} + \underbrace{\frac{Q_{net}}{\rho_0 c_p}}_{E} \underbrace{+ < \nabla_h \cdot (A_h \nabla_h T) >}_{F} \tag{5}$$

where

$$H = \int_{-h}^{0} T dz \tag{6}$$

is the local heat content stored in the whole water column, $<>= \int_{-h}^{0} dz$, T is the model temperature, Q_{net} is the net surface heat flux, ρ_0 is the reference water density, c_p is the specific heat of water, u, v, w are the eastern, northern and vertical components of the model velocity, A_h is the horizontal eddy diffusivity coefficient, and $\nabla_h = (\frac{\partial}{\partial x}, \frac{\partial}{\partial y})$. The nonlocal processes associated with horizontal and vertical advection and horizontal mixing are represented by terms B-D and F on the right hand side of the equation (5). The time-integrated heat balance at SB3 is discussed below in two frequency bands by filtering the terms in (5): a low-frequency band with periods of >30 days and a high-frequency band with periods of 1∼30 days. The change in the heat content due to the horizontal mixing in the model is small and is not discussed further.

The time-integrated heat and salt budgets in the low frequency band are shown in Figure 14. The balances at the end of the time series indicate the relative contributions of each term integrated over the study period. The heat budget during the study period (Figure 14a) is dominated by cooling of the water column due to vertical advection (∼-750°C m, red curve), i.e. upwelling, and warming due to horizontal advection (∼600°C m, the green and blue curves) and surface heat input (∼170°C m). The same basic balance also applies to the salinity budget (Figure 14b). In this case, on average, salty water (∼ 80 psu m) is upwelled, tending to increase the salinity of the water column, while horizontal advection (∼ -60 psu m) and the surface flux (∼ -20 psu m) act to freshen the water column. It is noticeable that during a warming period

in September (day 255-273, see Figure 9), cooling due to vertical advection is reduced, while horizontal advection continues to play a role in warming the water column. This is consistent with *Zhai et al.* [2007], who have already noted that the role played by advection associated with the first EOF mode of the observed subtidal currents at the mooring sites SB3 and MB1 during this time.

The heat balance in the high-frequency band (Figures 14b and d), however, shows that changes in the local heat (salt) content of the water column are associated mostly with vertical advection (i.e., upwelling/downwelling), and with horizontal advection acting oppositely but not dominating. This picture is confirmed by the correlations of advection terms B-D with the local heat content (term A). These take values of -0.26, -0.30, 0.62, respectively, indicating that the temporal variability of the local heat content is induced largely by vertical advection, with some contribution from the horizontal advection (all these correlations are statistically significant at the 1% level). A similar picture emerges for the salt budget. The correlations of terms B-D with the local salt content (term A) are -0.40, -0.21, and 0.56 respectively, indicating that the temporal variability of the local salt content is induced largely by the vertical advection, with some contribution from horizontal advection.

We have computed the heat budget for that part of the bay enclosed by a transect running due north from Ovens Point (Figure 1). Figure 15 shows the time integral of heat content inside this region, the heat flux through the surface and the advective heat flux through the transect across the mouth. The latter has been split into contributions from the tidal velocity and the 27 hour low-pass filtered velocity. This shows that the tides on average lead to a weak warming of the bay during this period, whereas the cooling associated with advection is dominated by the low-pass filtered flow, as expected. It should be noted, however, that at individual sites, the tides can play a locally more important role.

6. The depth-integrated momentum balance

We also perform an analysis of the depth-integrated momentum balance including the effect of stratification using the depth-integrated momentum equations defined as

$$\underbrace{\frac{\partial\langle u\rangle}{\partial t}}_{a} = \underbrace{-\langle\vec{u}\cdot\nabla u\rangle}_{b}\underbrace{+\langle fv\rangle}_{c}\underbrace{-\langle g\frac{\partial\eta}{\partial x}\rangle}_{d}\underbrace{-\langle\frac{1}{\rho_o}\frac{\partial P_b}{\partial x}\rangle}_{e}\underbrace{+\langle\nabla_h\cdot(A_m\nabla_h u)\rangle}_{f}\underbrace{+\langle\frac{\tau_x^s-\tau_x^b}{\rho_0}\rangle}_{g} \tag{7}$$

$$\underbrace{\frac{\partial\langle v\rangle}{\partial t}}_{a} = \underbrace{-\langle\vec{u}\cdot\nabla v\rangle}_{b}\underbrace{-\langle fu\rangle}_{c}\underbrace{-\langle g\frac{\partial\eta}{\partial y}\rangle}_{d}\underbrace{-\langle\frac{1}{\rho_o}\frac{\partial P_b}{\partial y}\rangle}_{e}\underbrace{+\langle\nabla_h\cdot(A_m\nabla_h v)\rangle}_{f}\underbrace{+\langle\frac{\tau_y^s-\tau_y^b}{\rho_0}\rangle}_{g} \tag{8}$$

where $P_b = g\int_z^0 \rho dz'$ is the density-driven internal pressure, (τ_x^s, τ_y^s) and (τ_x^b, τ_y^b) are the eastward and northward components of surface wind and bottom stresses respectively. Other symbols in (7) and (8) are defined in the Appendix. As in the previous section for the heat budget, here the time-integrated momentum balances at SB3 are also discussed for the high and low frequency bands.

At low frequencies (Figures 16a and c), the Coriolis (red) and momentum advection terms (dashed red) play an important role and effectively balance the combined effect of the surface minus bottom stress (black) and the pressure gradient term (blue), suggesting a modified geostrophic balance not unlike that in the arrested topographic wave (Csanady, 1978). By contrast, at high frequencies (Figures 16b and d), the dominant balance is between the wind minus the bottom stress (black) and the combined pressure gradient (blue), although the momentum advection and Coriolis terms do sometimes make a contribution. Repeating the analysis, but using the model results with the uniform temperature and salinity experiment (Exp-Baro) leads to similar results at both low and high frequency for the eastward (u) momentum equation, but reveals differences at low frequency for the northward (v) momentum equation. The latter is associated with the fact that the mean flow at SB3 is in the opposite direction in the control run with stratification, compared to the barotropic run, and an issue to be discussed further in a later paper.

7. Summary and discussion

Forced by tides, surface wind stress, remotely generated waves, net surface heat flux and diagnosed surface freshwater flux, the nested-grid ocean circulation modelling system simulates the circulation and thermal structure in Lunenburg Bay (LB) in the summer and fall 2003. The spatial and temporal variability of the simulated temperature and salinity is mainly associated with the wind-induced upwelling and downwelling, with some contribution from tidal advection and surface fluxes. The simulated currents show a strong baroclinic throughflow over the deep water region outside Lunenburg Bay that shows strong day-to-day variations associated with the wind.

The good agreement between the simulated and observed surface elevations indicates that the inner model of the nested-grid system reproduces very well the observed surface elevations at 5 locations in the study region. The inner model also captures the observed variations of temperature and salinity at three sites in LB. The simulated semi-diurnal M_2 tidal current ellipses compare reasonably well with those derived from the observations, with the misfits generally smaller than 1 cm s^{-1} at the three sites. The simulated non-tidal currents generally agree with the observations, but have less temporal variability. The inner model reproduces the spatial pattern of the first EOF mode of the subtidal currents, but tends to underestimate the first mode coefficient during strong wind events.

Based on the agreement between the simulated and observed fields, the model results are used to estimate the heat, salt and momentum balances at SB3. At low frequency (time scales larger than 30 days), the local heat and salt balance is dominated by cooling (increasing saltiness) due to vertical advection and warming (freshening) due to horizontal advection and the surface heat (freshwater) input. In the high-frequency band (time scales shorter than 30 days), the changes in local heat (salt) content are mainly controlled by vertical advection, indicating the effects of local upwelling and downwelling. Integrated over the bay as a whole, the tides are found to lead to a weak warming effect, although locally the tides can have a more important role in

the heat/salt balance. The depth-integrated momentum balance in the low frequency band suggests a modified geostrophic balance, but with wind minus bottom stress and also advection playing a role. The momentum balance in the high-frequency band is dominated by the pressure term and the wind minus bottom stress, consistent with barotropic dynamics.

Acknowledgments

The authors wish to thank Liang Wang, Jun Zhao, Mike Dowd, Keith Thompson, John Cullen and Marlon Lewis for their useful suggestions and comments; Alex Hay and Douglas Schillinger for providing the buoy, ADCP and PT sensor measurements in Lunenburg Bay, Richard Davis for providing the optical and hydrographic measurements in the bay; Brian Petrie for providing the hydrographic measurements at station 2 along Halifax line; and Blair Greenan for providing the minilog temperature measurements in the bay. This study is part of the CMEP project funded by the Canadian Foundation for Climate and Atmospheric Studies (CFCAS). Authors R.J.G and J.S. are also supported by the NSERC, MARTEC (a Halifax-based company), and MSC through the NSERC/MARTEC/MSC Industrial Research Chair in "Regional Ocean Modelling and Prediction".

Appendix: The CANDIE model

The governing equations used in the CANDIE model are the same as those considered by *Sheng and Wang* [2004]. To facilitate physical interpretation, the equations are expressed in Cartesian coordinates

$$\frac{\partial u}{\partial t} + \nabla \cdot (\vec{u}u) - fv = -\frac{1}{\rho_0}\frac{\partial p}{\partial x} + \frac{\partial}{\partial z}(K_m \frac{\partial u}{\partial z}) + \nabla_h \cdot (A_m \nabla_h u), \tag{A1}$$

$$\frac{\partial v}{\partial t} + \nabla \cdot (\vec{u}v) + fu = -\frac{1}{\rho_0}\frac{\partial p}{\partial y} + \frac{\partial}{\partial z}(K_m \frac{\partial v}{\partial z}) + \nabla_h \cdot (A_m \nabla_h v), \tag{A2}$$

$$\nabla \cdot \vec{u} = 0, \tag{A3}$$

$$\frac{\partial T}{\partial t} + \nabla \cdot (\vec{u}T) = \frac{\partial}{\partial z}(K_h \frac{\partial T}{\partial z}) + \nabla_h \cdot (A_h \nabla_h T), \tag{A4}$$

$$\frac{\partial S}{\partial t} + \nabla \cdot (\vec{u}S) = \frac{\partial}{\partial z}(K_h \frac{\partial S}{\partial z}) + \nabla_h \cdot (A_h \nabla_h S), \tag{A5}$$

$$\rho = \rho(T, S, p), \tag{A6}$$

$$p = g\int_z^\eta \rho dz, \tag{A7}$$

$$\frac{\partial \eta}{\partial t} = -\frac{\partial}{\partial x}\int_{-h}^{\eta} u dz - \frac{\partial}{\partial y}\int_{-h}^{\eta} v dz, \tag{A8}$$

where u, v, w are eastward, northward, and vertical components of the velocity vector, respectively; p is pressure; ρ is density calculated from the temperature T and salinity S; f is the Coriolis parameter; g is the gravitational acceleration; ρ_o is a reference density; h is water depth; K_m and K_h are the vertical eddy viscosity and diffusivity coefficients; and A_m and A_h are the horizontal eddy viscosity and diffusivity coefficients. The vector operators ∇, ∇_h and $\vec{u}$ are defined by

$$\nabla = (\frac{\partial}{\partial x}, \frac{\partial}{\partial y}, \frac{\partial}{\partial z}), \qquad \nabla_h = (\frac{\partial}{\partial x}, \frac{\partial}{\partial y}), \qquad \vec{u} = (u, v, w). \tag{A9}$$

References

Bowden, K. F. (1983), *Physical oceanography of coastal waters,* Halsted Press, New York, 302 pp.

Brink, K. H., J. S. Allen, and R. L. Smith (1978), A study of low-frequency fluctuations near the Peru Coast, *J. Phys. Oceanogr.*, **8**, 1025-1041.

Clarke, A. J. (1977), Observational and numerical evidence for wind-forced coastal trapped long waves, *J. Phys. Oceanogr.*, **7**, 231-247.

Crèpon M., C. Richez, and M. Chartier (1984): Effects of coastline geometry on upwellings, *J. Phys. Oceanogr., 8,* 1365-1382.

Csanady, G.T. (1974), Spring thermocline behavior in Lake Ontario during IFYGL, *J. Phys. Oceanogr.*, **4**, 425-445.

Csanady, G.T. (1978), The arrested topographic wave, *J. Phys. Oceanogr.*, **8**, 47-62.

Davies, A. M., and R. A. Flather (1978), Computing extreme meteorologically induced currents with application to the northwest European continental shelf, *Cont. Shelf Res.,* 7, 643-683.

Davidson, F., R. J. Greatbatch, and B. deYoung (2001), Asymmetry in the response of a stratified coastal embayment to wind forcing, *J. Geophys. Res.*, 106, 7001-7016.

deYoung, B., T. Otterson, and R. J. Greatbatch (1993), The local and nonlocal response of Conception Bay to wind forcing, *J. Phys. Oceanogr.*, 23, 2636-2649.

Dietrich, D. E. (1997), Application of a modified Arakawa 'a' grid ocean model having reduced numerical dispersion to the Gulf of Mexico circulation, *Dyn. Atmos. and Oceans*, **27**, 201-217.

Durski, S. M., S. M. Glenn, and D. B. Haidvogel (2004), Vertical mixing schemes in the coastal ocean, Comparison of the level 2.5 Mellor-Yamada scheme with an enhanced version of the K profile parameterization, *J. Geophys. Res.,* 109, C01015, doi:10.1029/2002JC001702.

Emery, W.J. and R.E. Thomson (1998), *Data Analysis Methods in Physical Oceanography*, Elsevier, 638 pp.

Gill, A. E. (1982), *Atmosphere-Ocean Dynamics*, Academic Press, New York, 662 pp.

Hachey, H.B. (1937), Ekman's theory applied to water replacement on the Scotian shelf, *Proc. N. S. Inst. Sci.,* 19, 264-276.

Large, W. G., J. C. McWilliams, and S. C. Doney (1994), Oceanic vertical mixing: a review and a model with a nonlocal boundary layer parameterization, *Review of Geophysics, 32,* 363-403.

Lu, Y., D. G. Wright, and D. Brickman (2001), Internal tide generation over topography: experiments with a free-surface z-level ocean model, *J. Atmos. and Ocean. Tech., 18*, 1076-1091.

Orlanski, I., 1976: A simple boundary condition for unbounded hyperbolic flows. *J. Comput. Phys.*, **21**, 251-269.

Paulson, C. A. and J. J. Simpson (1977), Irradiance Measurements in the Upper Ocean, *J. Phys. Oceanogr., 7*, 952-956.

Pawlowicz, R., B. Beardsley, and S. Lentz (2002), Classical tidal harmonic analysis including error estimates in MATLAB using T_TIDE, *Computers and Geosciences*, **28**, 929-937.

Petrie, B., B. J. Topliss and D. G. Wright (1987), Coastal upwelling and eddy development off Nova Scotia, *J. Geophys. Res., 29,* 12,979-12,991.

Sheng, J., and L. Wang (2004), Numerical study of tidal circulation and nonlinear dynamics in Lunenburg Bay, Nova Scotia, *J. Geophys. Res., 109,* C10018, doi:10.1029/2004JC002404.

Sheng, J., J. Zhao and L. Zhai (2007), An examination of circulation, dispersion and connectivity in Lunenburg Bay of Nova Scotia using observations made by the

Canadian ocean observatory and a nested-grid circulation model, *Journal of Marine Systems.*, (submitted).

Smagorinsky, J. (1963), General circulation experiments with the primitive equation. I. The basic experiment. *Monthly Weather Review*, **21**, 99-165.

Sturley, D. R. M., and A. J. Bowen (1996), A model for contaminant transport in Lunenburg Bay, Nova Scotia, *The Science of the Total Environment*, 179, 161-172.

Thompson, K. R., D. E. Kelley, D. Sturley, B. Topliss, and R. Leal (1998), Nearshore circulation and synthetic aperture radar: an exploratory study, *Int. J. Remote Sensing, 19*, 1161-1178.

Thompson, K. R., and J. Sheng (1997), Subtidal circulation on the Scotian Shelf: Assessing the hindcast skill of a linear, barotropic model, *J. Geophys. Res., 102*, 24987-25003.

Thuburn, J (1996), Multidimensional flux-limited advection schemes, *J. Comput. Phys.*, **123**, 74-83.

Wang, L., J. Sheng, A. E. Hay, and D. J. Schillinger (2007), Storm-induced circulation in Lunenburg Bay of Nova Scotia, *J. Phys. Oceanogr.,* (in press).

Zhai, L., J. Sheng and R. J. Greatbatch (2007), Observations of the dynamical response of a coastal embayment to wind, tide, and buoyancy forcing. *Cont. Shelf Res.*, submitted.

Received ; revised ; accepted .

Table 1. List of four numerical experiments forced by different combination of wind (W), tides (T), and buoyancy forcing associated with sea surface heat and freshwater fluxes (B).

Name of run	External forcing	Temperature and Salinity
Exp-Control	W+T+B	non-uniform
Exp-Wind	W+B	non-unform
Exp-Tide	T+B	non-uniform
Exp-Baro	W	uniform

Table 2. Comparison of observed and simulated tidal elevations at five sites in Lunenburg Bay and adjacent two coves. In the Table, ΔH and $\Delta\phi$ represent model errors in simulating amplitudes and phases.

	Amplitude (cm)			Phase (°)		
Station	Observed	Modeled	ΔH	Observed	Modeled	$\Delta\phi$
			M_2			
SB2	62.29	62.21	0.08	197.27	198.22	-2.09
SB3	61.47	61.94	-0.47	197.10	198.21	-1.11
H	62.46	62.23	0.23	194.71	198.23	-3.52
B	60.67	61.95	-1.28	197.73	200.84	-3.11
M	44.21	44.26	-0.05	232.54	244.94	-12.40
			S_2			
SB2	16.22	16.82	-0.60	26.72	13.33	13.39
SB3	16.06	16.75	-0.69	26.78	13.35	13.43
H	16.15	16.81	-0.66	24.21	13.31	11.00
B	15.92	16.63	-0.71	31.09	16.65	14.44
M	9.89	10.42	-0.53	69.70	73.44	-3.74
			N_2			
SB2	13.82	13.93	-0.11	50.87	56.62	-5.75
SB3	13.55	13.88	-0.33	49.93	56.65	-6.72
H	14.09	13.94	0.15	48.69	56.63	-7.94
B	13.08	13.83	-0.75	54.66	59.49	-4.83
M	9.84	10.42	-0.58	95.82	73.44	22.38

Table 3. A comparison of observed and simulated M_2 tidal current ellipses parameters at three different depths of sites SB2, SB3 and MB1 in Lunenburg Bay.

	Semi-major (cm)		Orientation (degree)		Phase (degree)	
Station	Observed	Modeled	Observed	Modeled	Observed	Modeled
SB2 (3.5m)	2.49	2.61	176.87	174.28	130.92	157.18
SB2 (5.5m)	2.43	2.20	165.57	171.87	116.21	135.23
SB2 (7.5m)	1.91	1.78	160.25	152.84	101.26	134.42
SB3 (3.5m)	3.86	4.39	157.94	160.89	140.65	156.42
SB3 (6.5m)	4.29	4.04	158.49	165.49	125.43	134.90
SB3 (10.5m)	5.11	3.98	162.51	168.48	118.49	105.11
MB1 (3.5m)	4.07	5.00	135.36	136.25	97.18	104.36
MB1 (6.5m)	4.25	4.17	139.62	139.63	94.70	101.85
MB1 (10.5m)	2.80	1.63	165.58	168.05	70.45	80.37

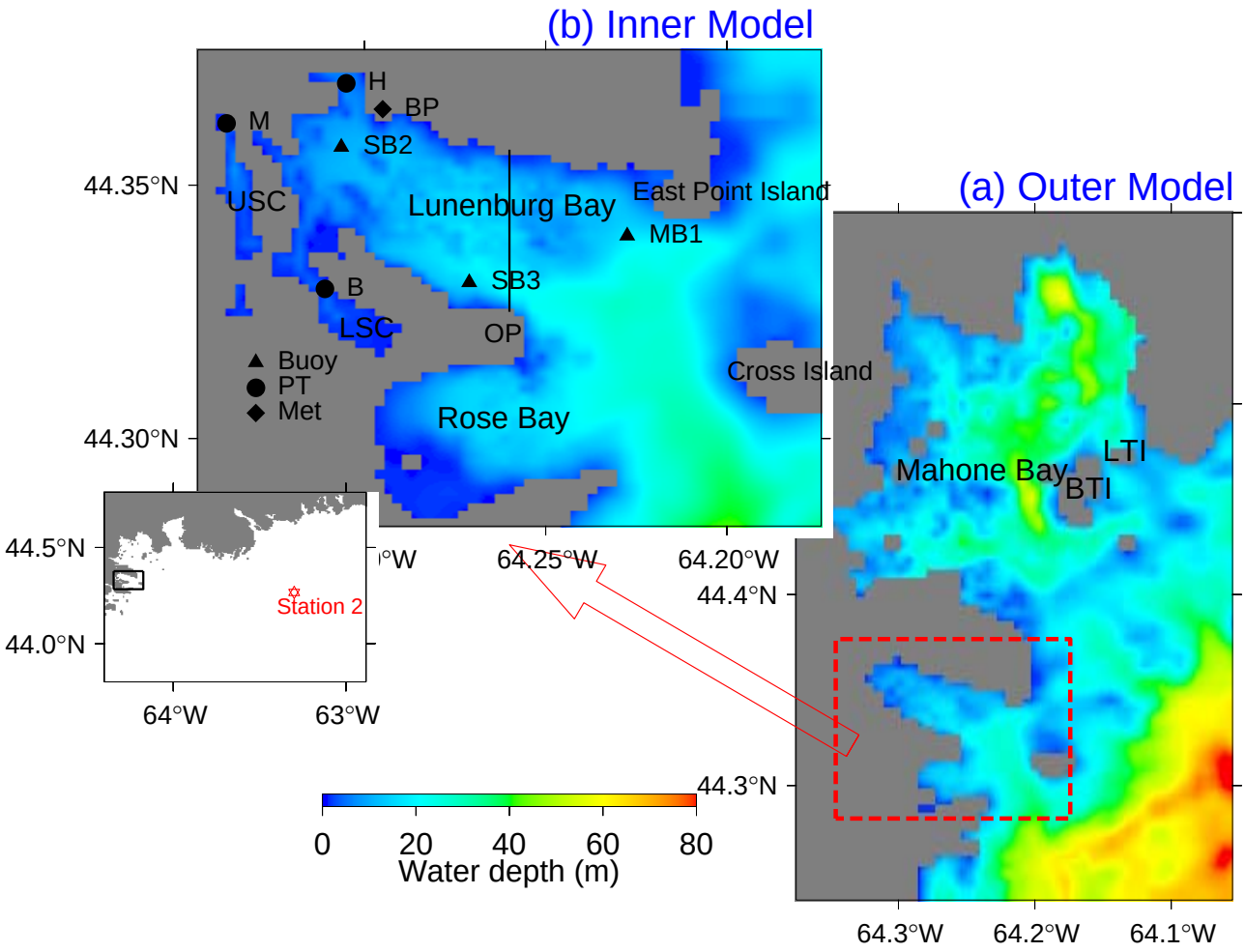

Figure 1. Major bathymetry features within the domains of (a) the outer model and (b) the inner model of the nested-grid modelling system for Lunenburg Bay. Abbreviations are used for Big Tancook Island (BTI), Cross Island (CI), Upper South Cove (USC), Lower South Cove (LSC), and Ovens Point (OP). The solid triangles denote the buoy locations. The solid circles denote the locations of pressure-temperature (PT) sensors. The solid diamond denotes the meteorological station. Inset shows a large area that covers inner Scotian Shelf, and Station 2 is marked by a star.

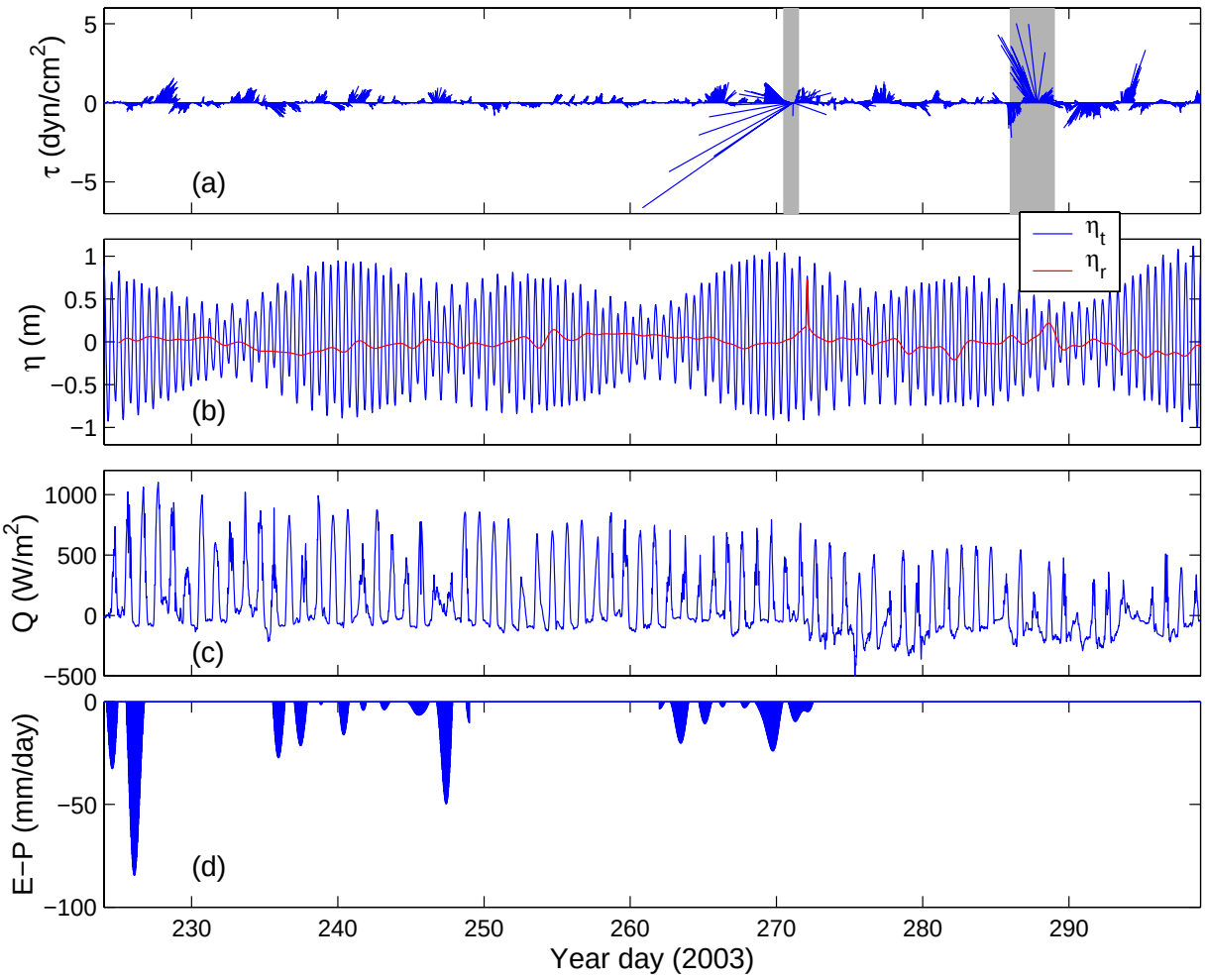

Figure 2. Time series of (a) wind stress, (b) tidal elevations η_t (blue line) and remotely generated waves η_r (red line), (c) net sea surface heat flux, and (d) diagnosed sea surface freshwater flux $(E - P)$ from day 224 (August 13) to 299 (October 27) in 2003.

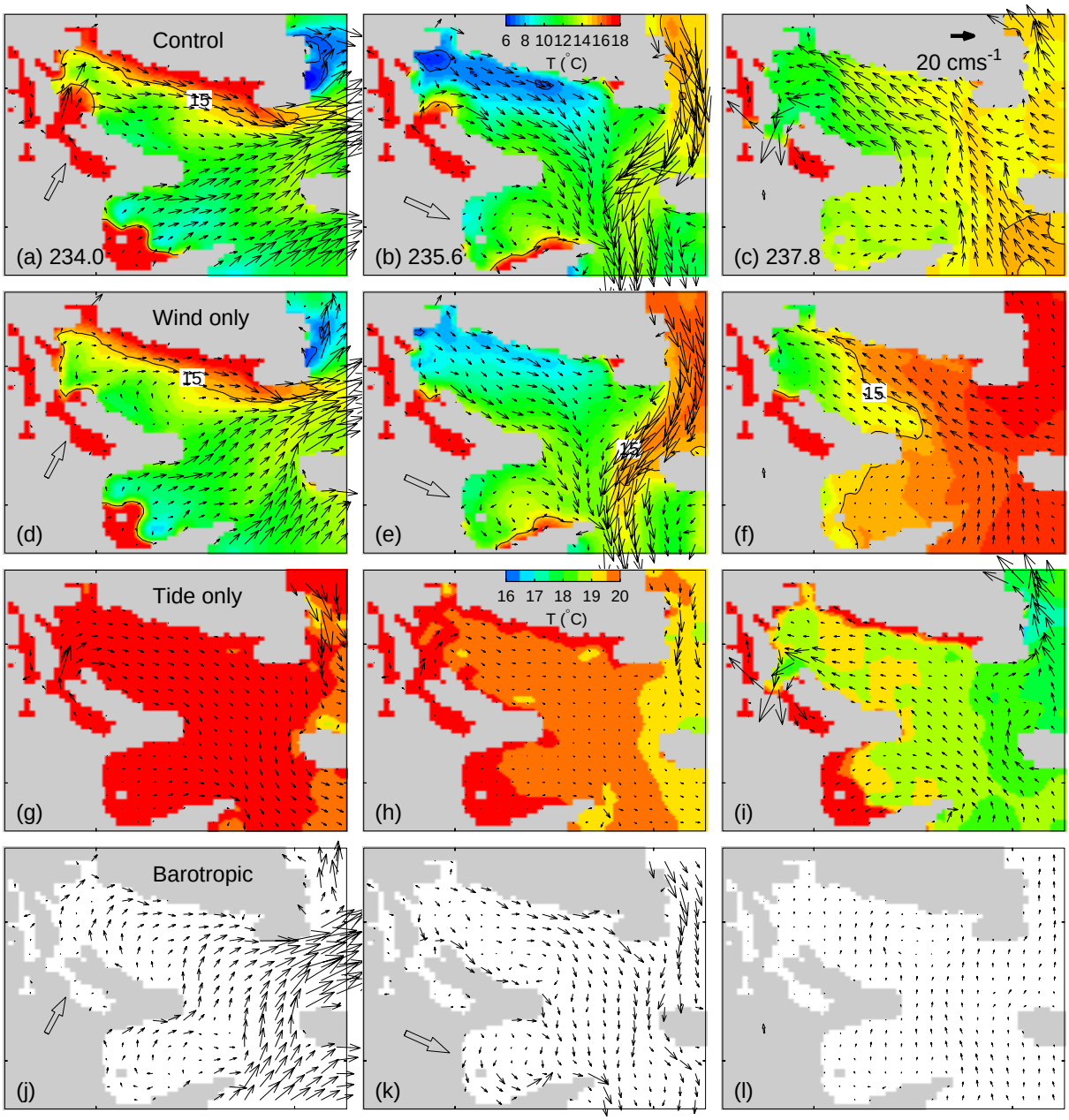

Figure 3. Modeled near-surface (3.5 m) currents and temperatures at day (a) 234.0, (b) 235.6, and (c) 237.8 in the control run; (d-f) from the experiment forced by wind only (Exp-Wind); (g-i) from the experiment forced by tides only (Exp-Tide); (j-l) from the experiment forced by wind only with temperature and salinity set to be constant (Exp-Baro).

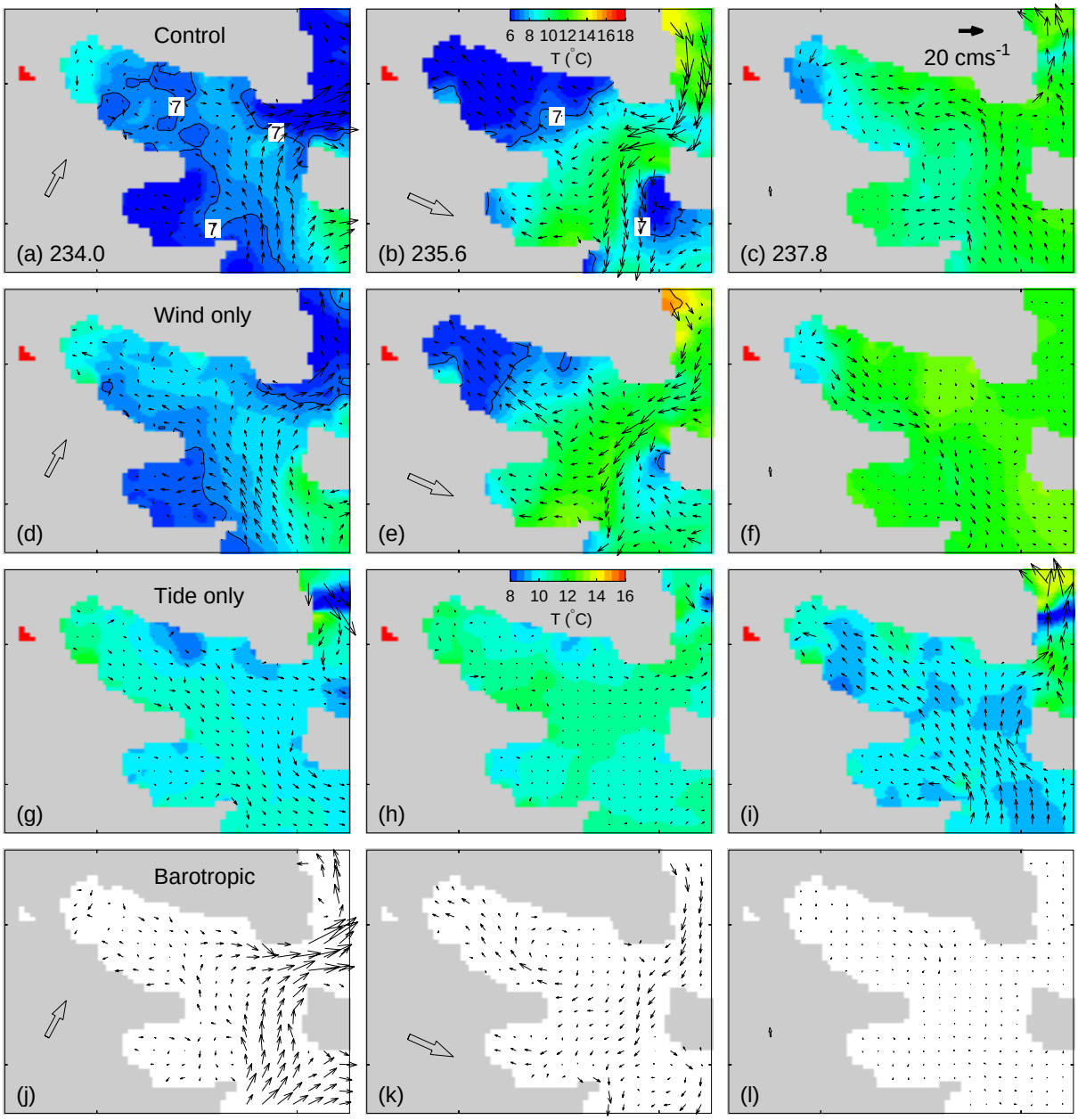

Figure 4. Modeled sub-surface (7.5 m) currents and temperatures at day (a) 234, (b) 235.6 and (c) 237.8 in the control run; (d-f) from the experiment forced by wind only (Exp-Wind); (g-i) from the experiment forced by tides only (Exp-Tide); (j-l) from the experiment forced by wind only with temperature and salinity set to be constant (Exp-Baro).

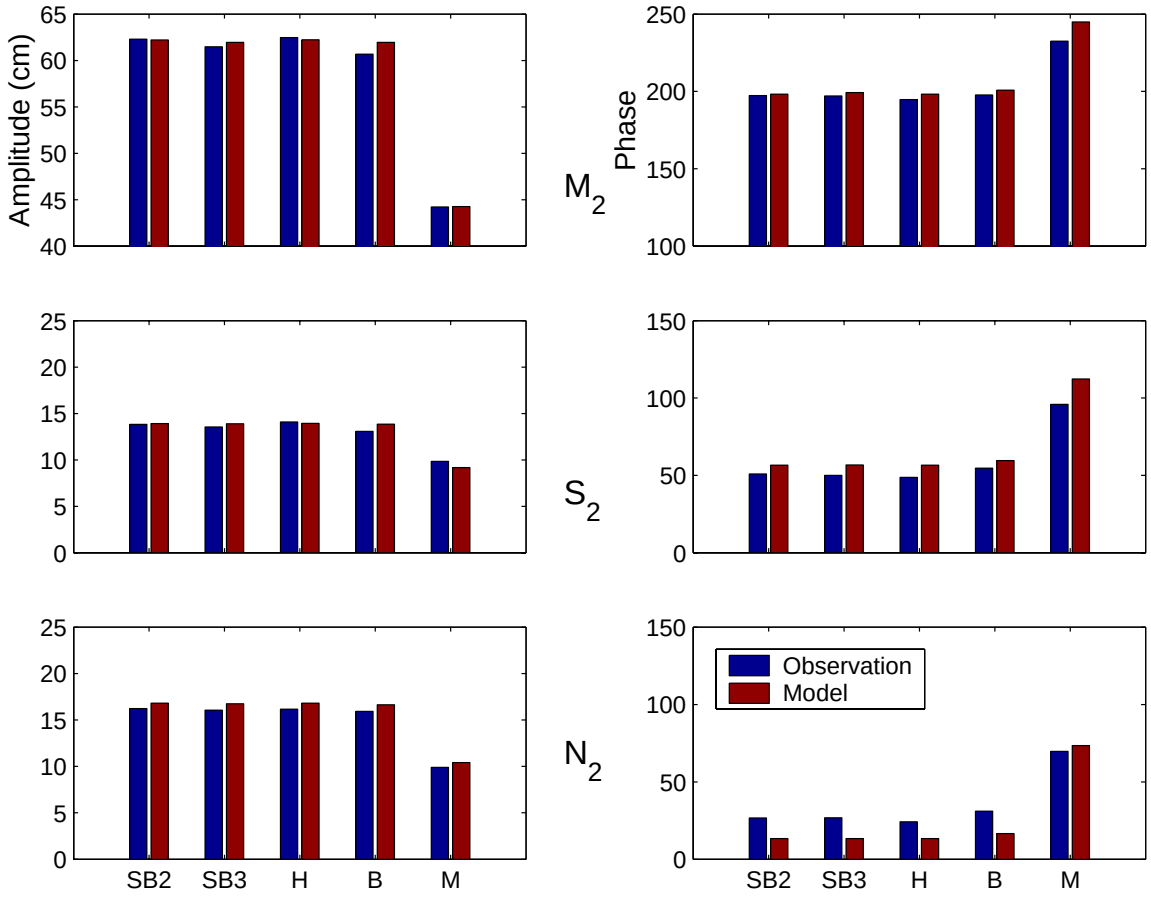

Figure 5. Comparison of observed and model calculated amplitudes and phases of M_2, S_2 and N_2 constituents of tidal elevations at sites SB2, SB3, and H in Lunenburg Bay, at site B in Lower South Cove, and at site M in Upper South Cove respectively.

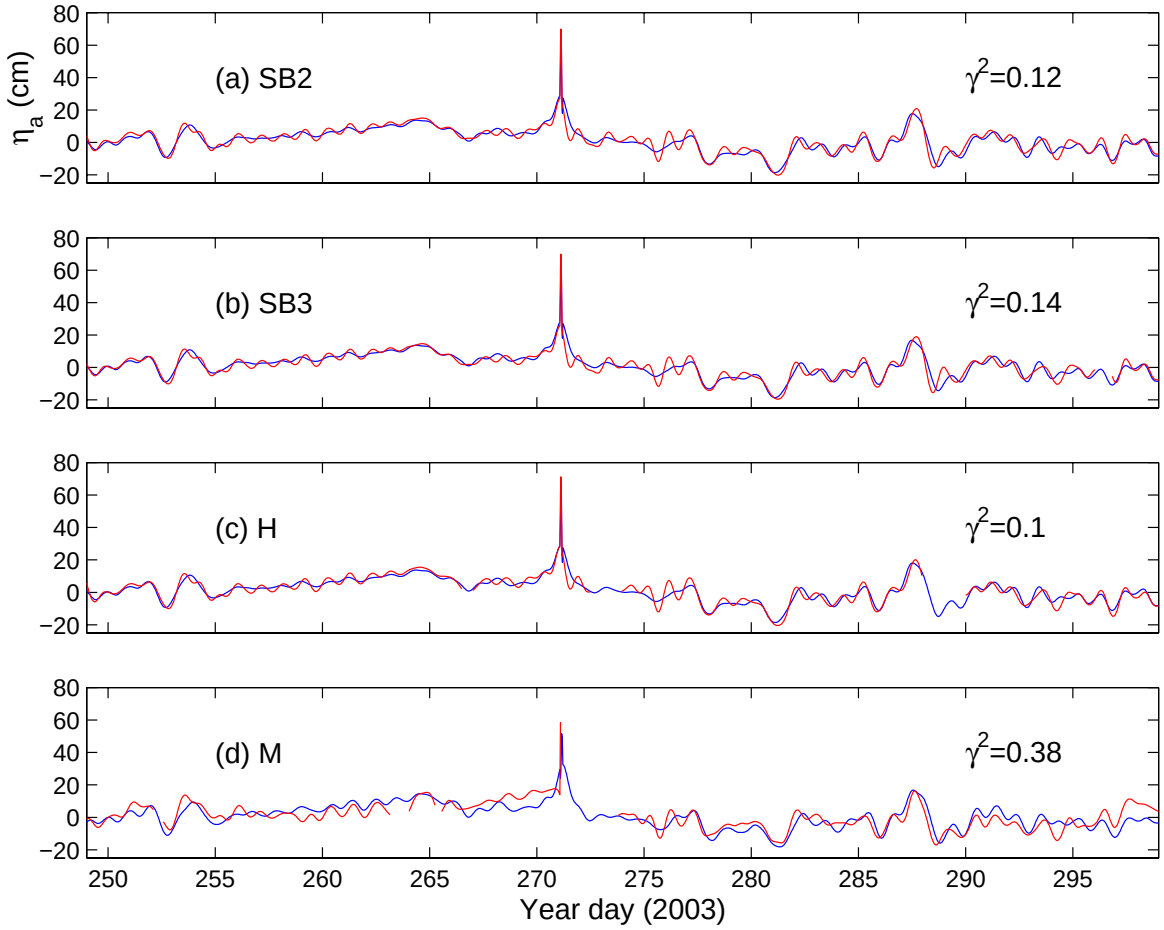

Figure 6. Comparison of observed and simulated non-tidal elevations at sites (a) SB2, (b) SB3, (c) H in Lunenburg Bay and at site (d) M in Upper South Cove. The simulated results are produced by the nested-grid inner model in the control run.

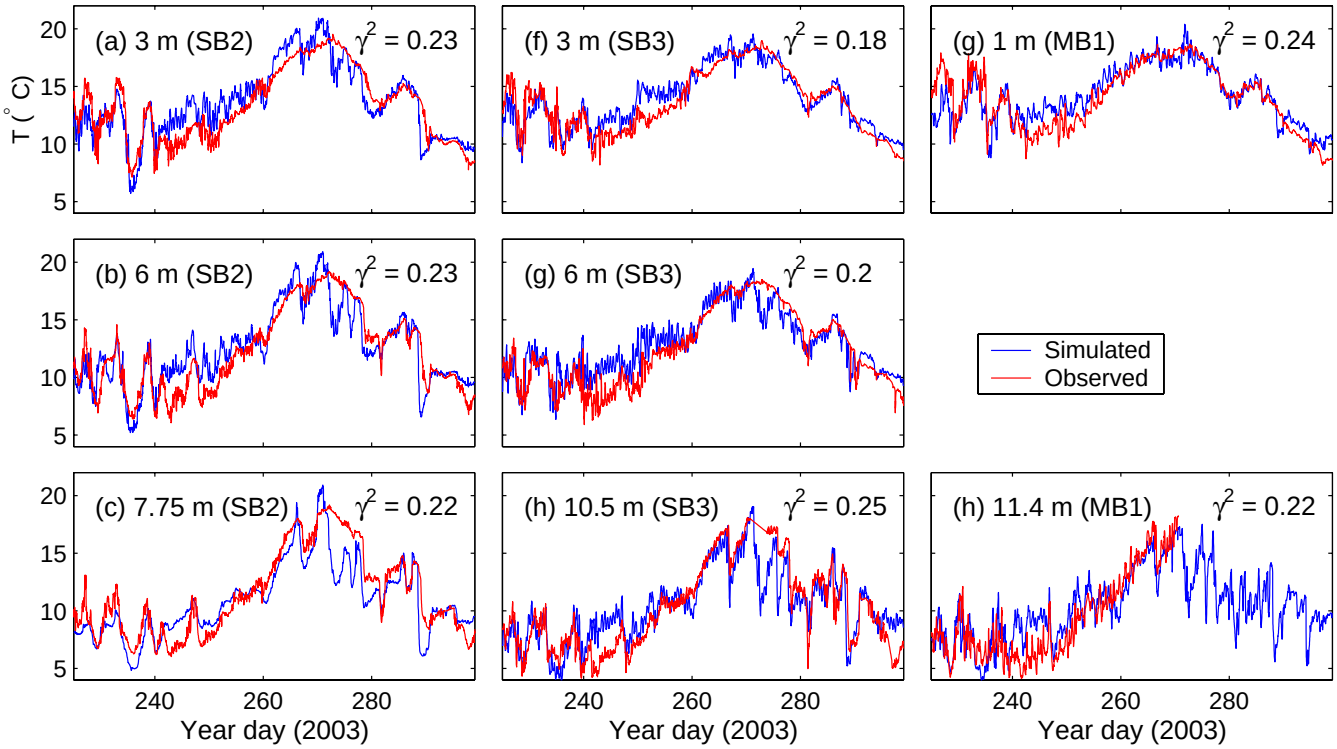

Figure 7. Comparison of observed and simulated temperatures at depths of 3, 6 and 7.5 m at site SB2 (left panels); at depths of 3, 6 and 10.5 m at site SB3 (middle panels), and at depths of 1, 11.4 m at site MB1 (right panels). The simulated results are produced by the nested-grid inner model in the control run.

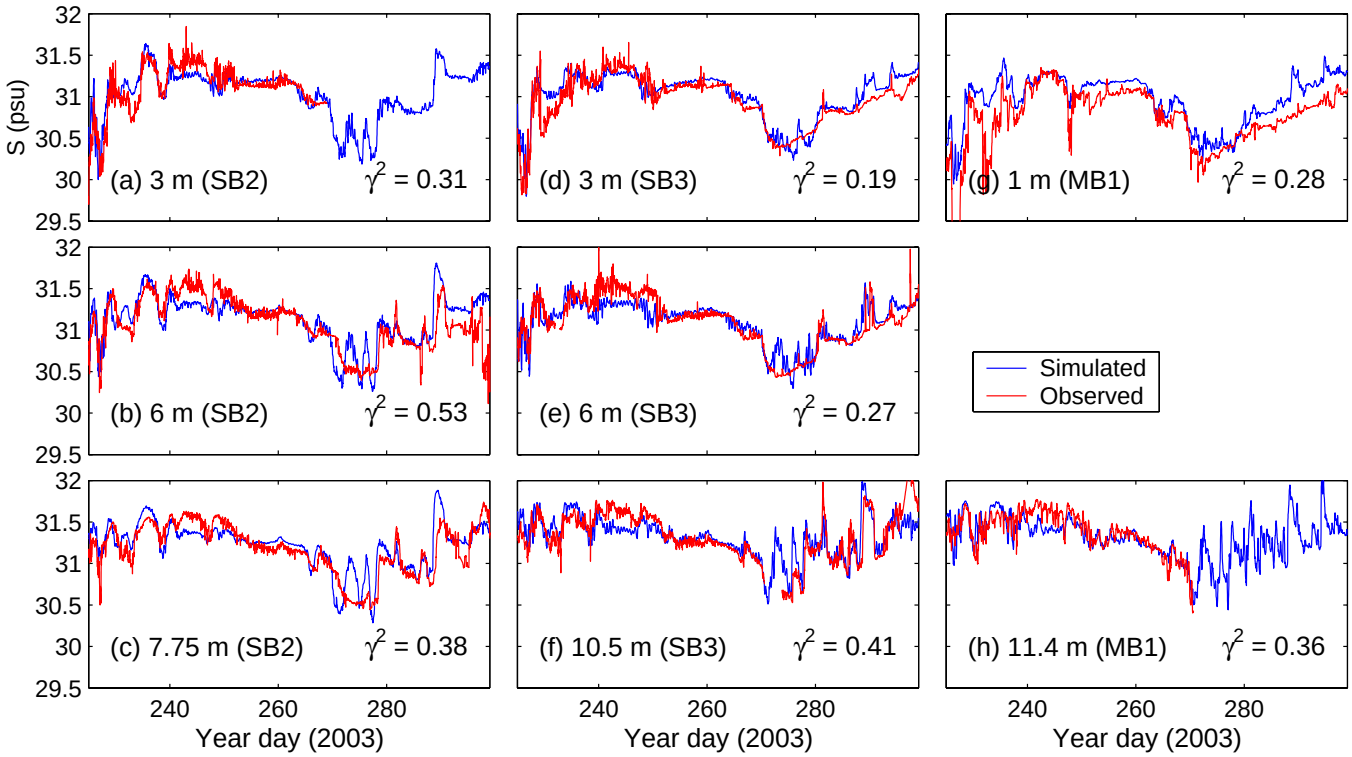

Figure 8. Comparison of observed and simulated salinities at depths of 3, 6, and 7.75 m at site SB2 (left panels); at depths of 3, 6 and 10.5 m at site SB3 (middle panels), and at depths of 1 and 11.4 m for site MB1 (right panels). The simulated results are produced by the nested-grid inner model in the control run.

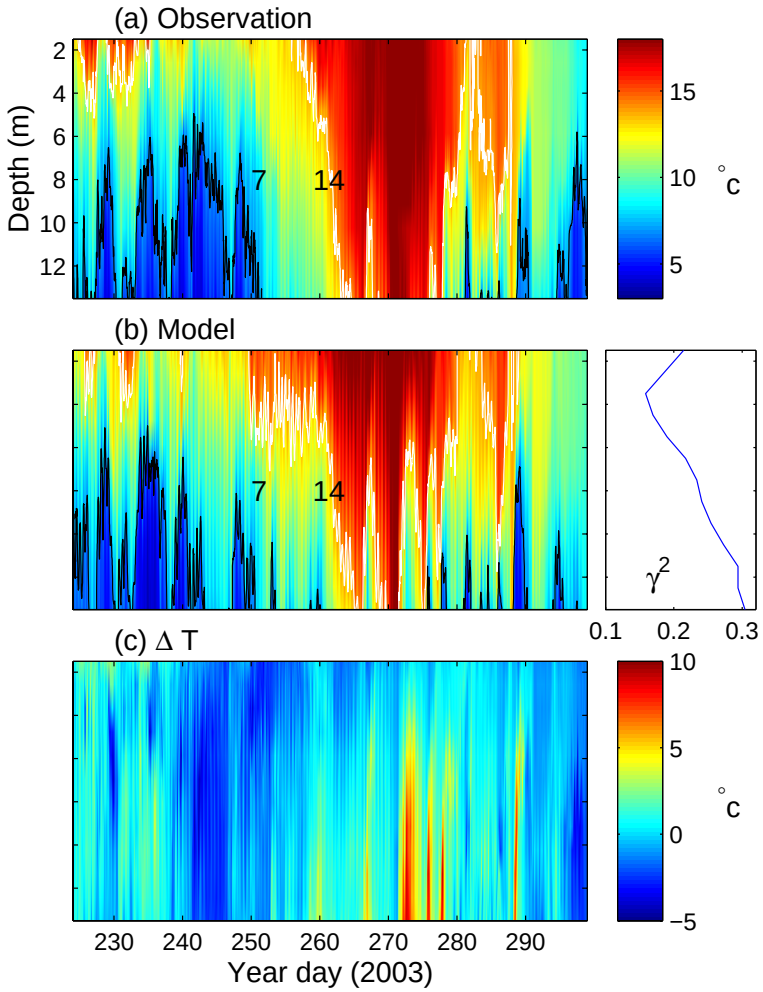

Figure 9. Time-depth distributions of (a) observed, (b) modeled, and (c) the difference, observed minus modeled temperatures at SB3. The observed temperaures were made by the minilog temperature recorders and the bottom pressure-temperature sensors at SB3. The simulated results are produced by the nested-grid inner model in the control run.

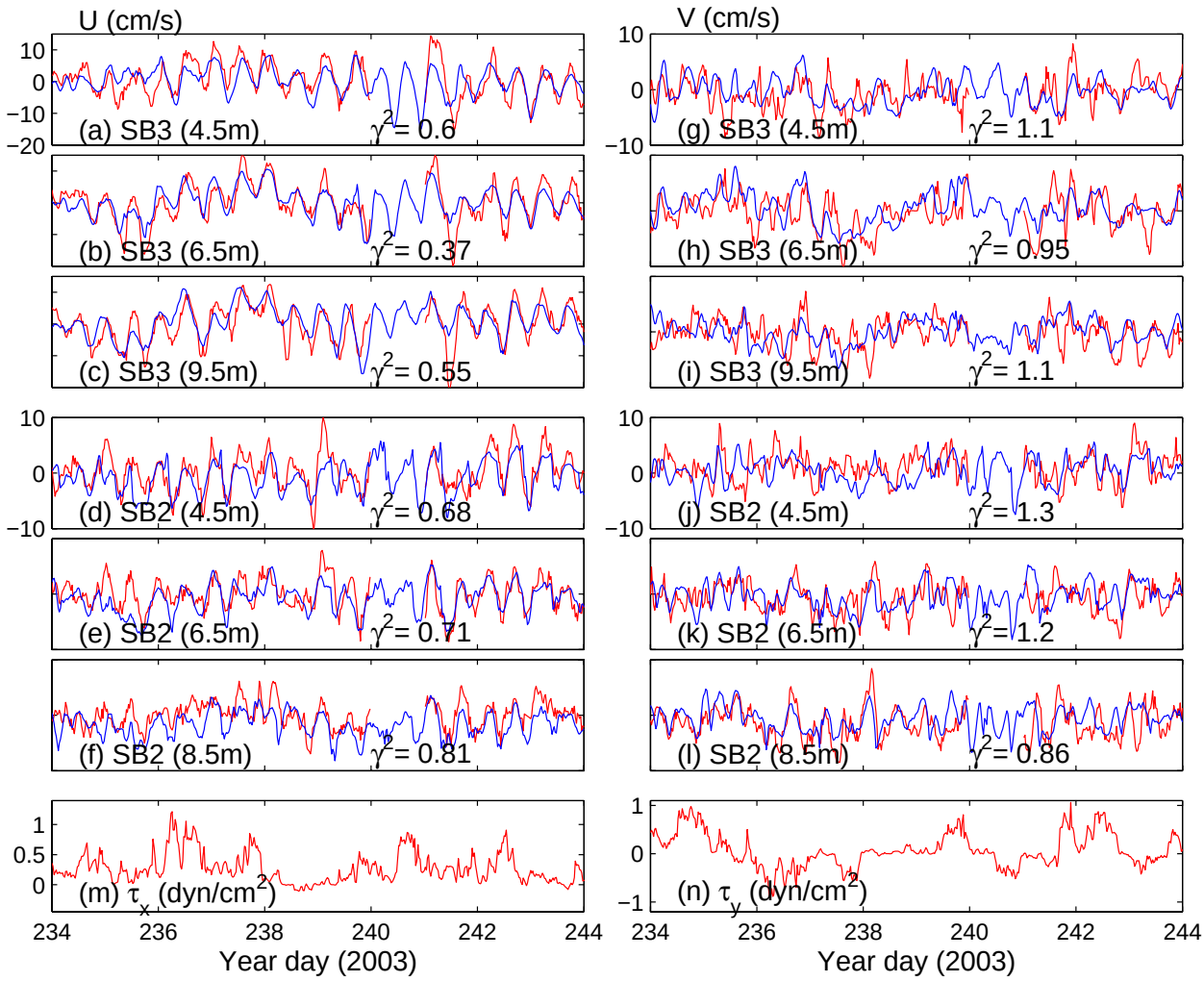

Figure 10. Comparison of eastward (left panels) and northward (right panels) components of observed (red) and simulated currents (blue) at depths of 4.5, 6.5 and 9.5 m at site SB3 (left panels), and those at depths of 4.5, 6.5 and 8.5 m at site SB2 (right panels) from day 234 to 244, 2003. Bottom two panels are (m) the eastward and (n) northward wind stress.

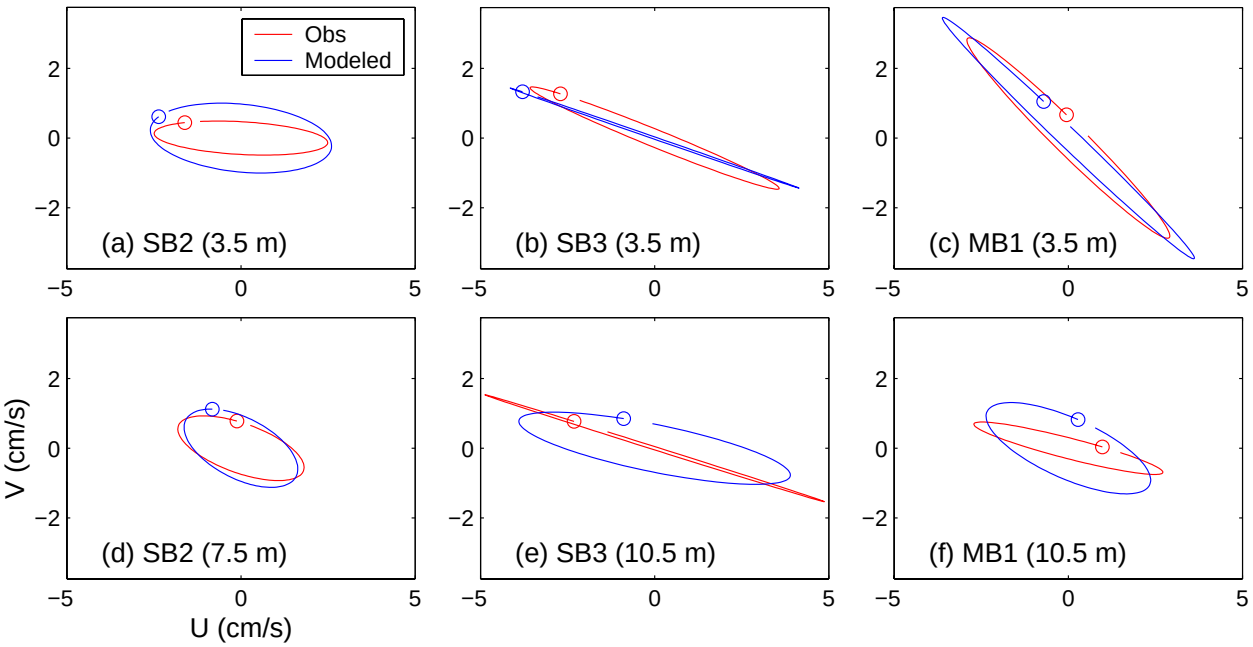

Figure 11. Comparison of the observed (red) and simulated (blue) M_2 tidal current ellipses at two different depths of (a, d) SB2, (b, e) SB3, and (c, f) MB1.

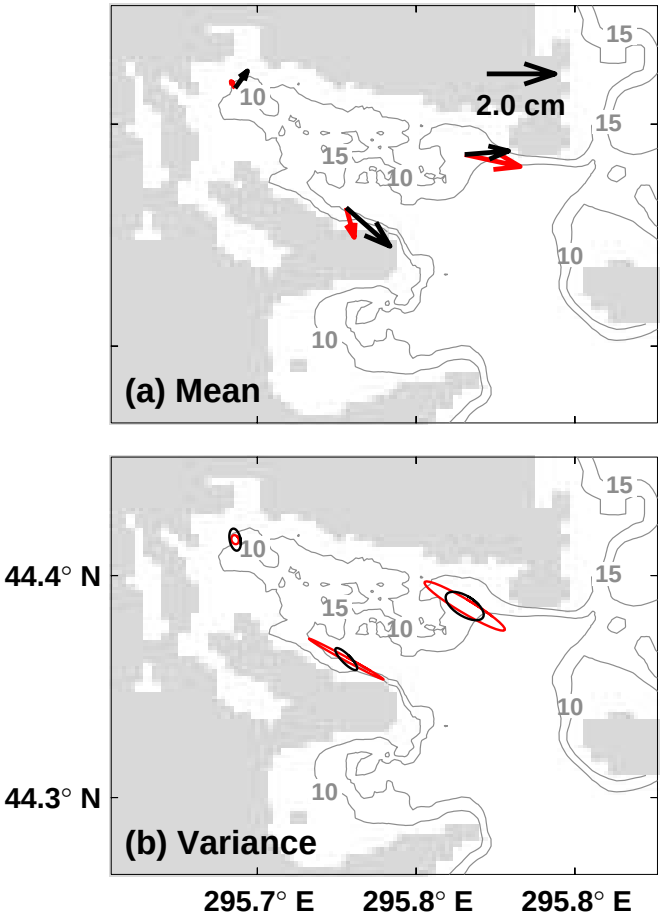

Figure 12. Comparison of observed (red) and simulated (blue) (a) means and (b) variances of near-surface sub-tidal currents at 4.5 m at three sites from day 266 to 292, 2003.

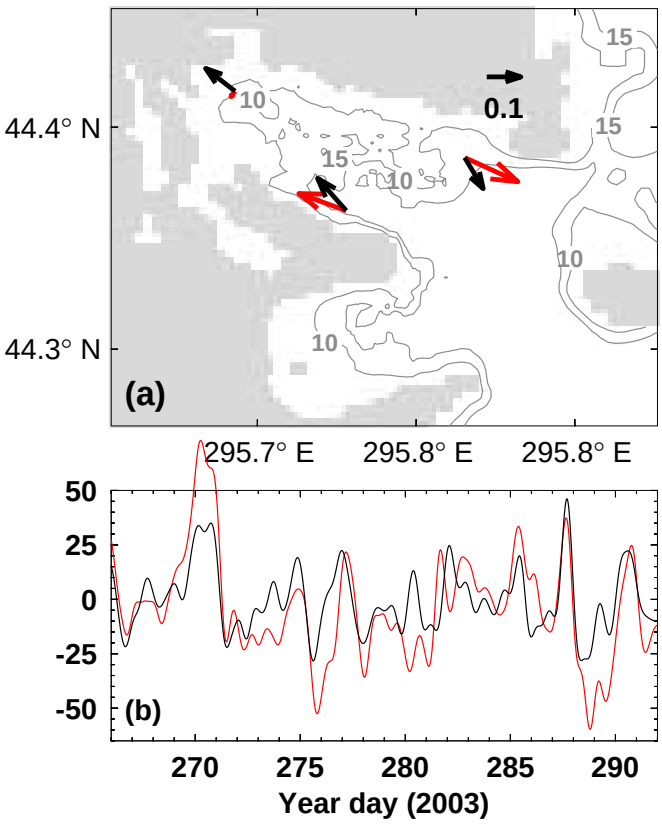

Figure 13. Principal component analysis of observed and simulated sub-tidal currents at 4.5 m: (a) the first EOF mode eigenvectors, (b) the first EOF mode coefficient of observed (red) and simulated (blue) currents at three sites.

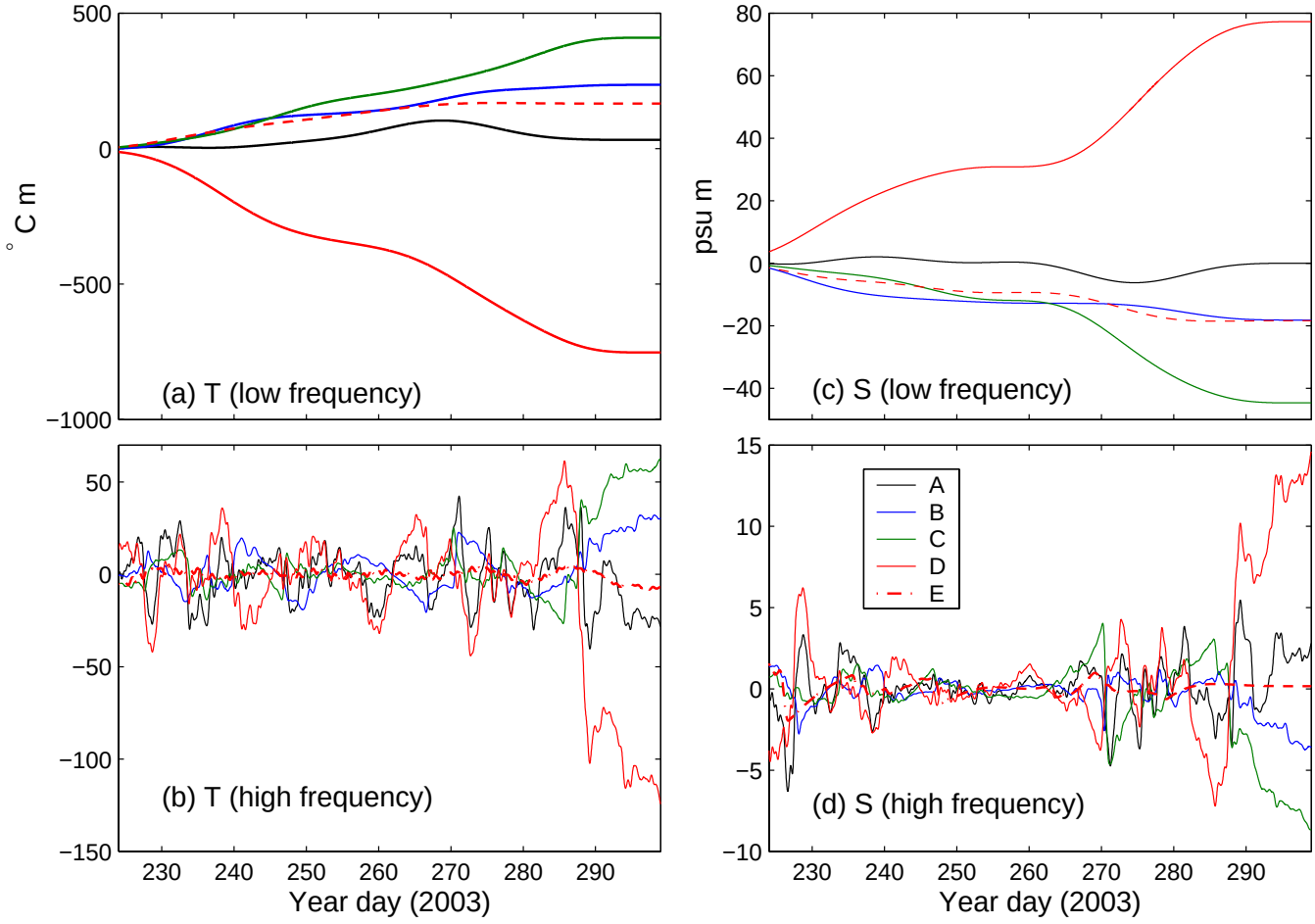

Figure 14. Time series of (a) the low-frequency and (b) high-frequency heat budgets, and (c) low-frequency and (d) high-frequency salt budgets at site SB3. Time-integrated heat (salt) content (A) is indicated by the black line, the eastward (B), northward (C) and vertical (D) advections by the blue, green and red lines, and the surface heating (E) by the dashed red line.

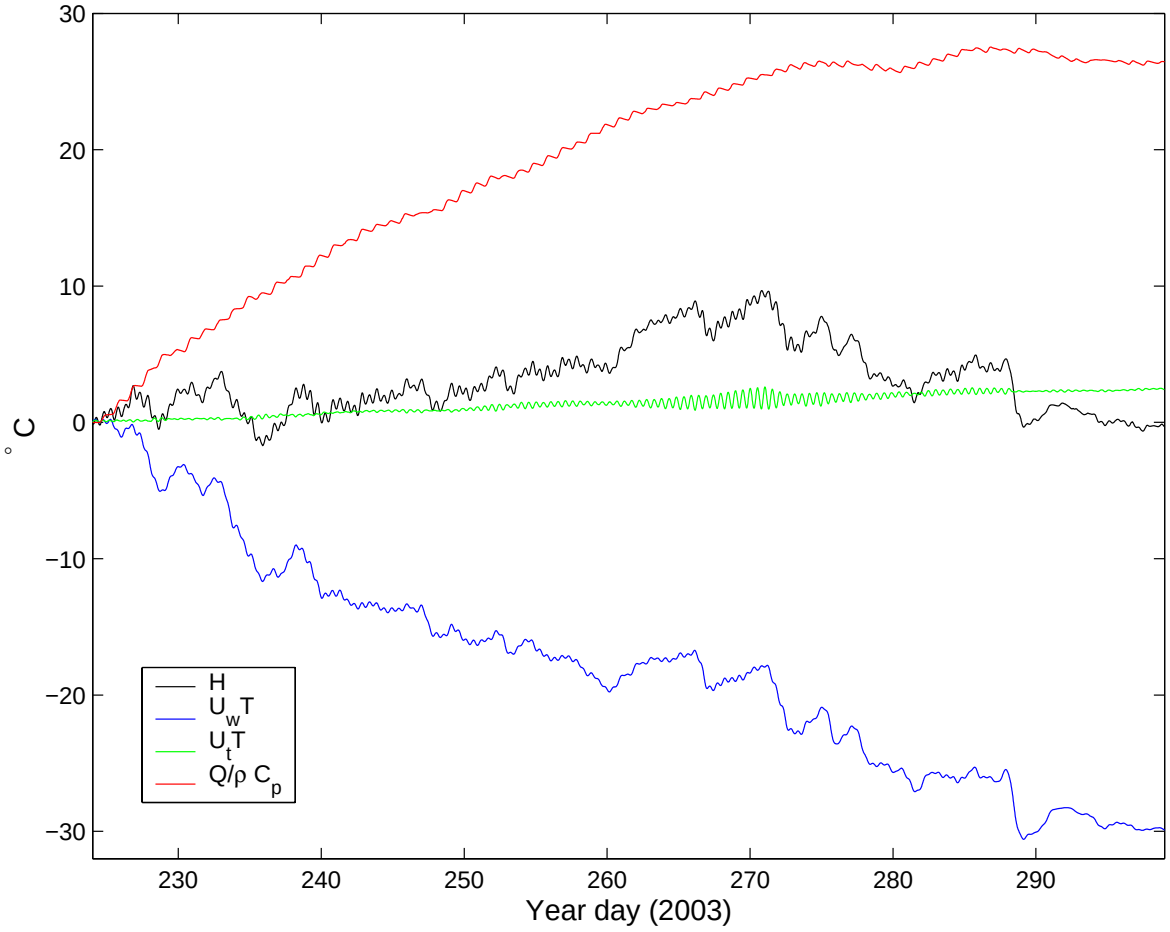

Figure 15. Time series of the time integral of the heat budget in LB enclosed by a transect running due north from Ovens Point. Time-integrated heat content is indicated by the black line, the advection induced by wind is indicated by the blue line, the advection induced by tides is indicated by the green line, and the surface heating by the red line.

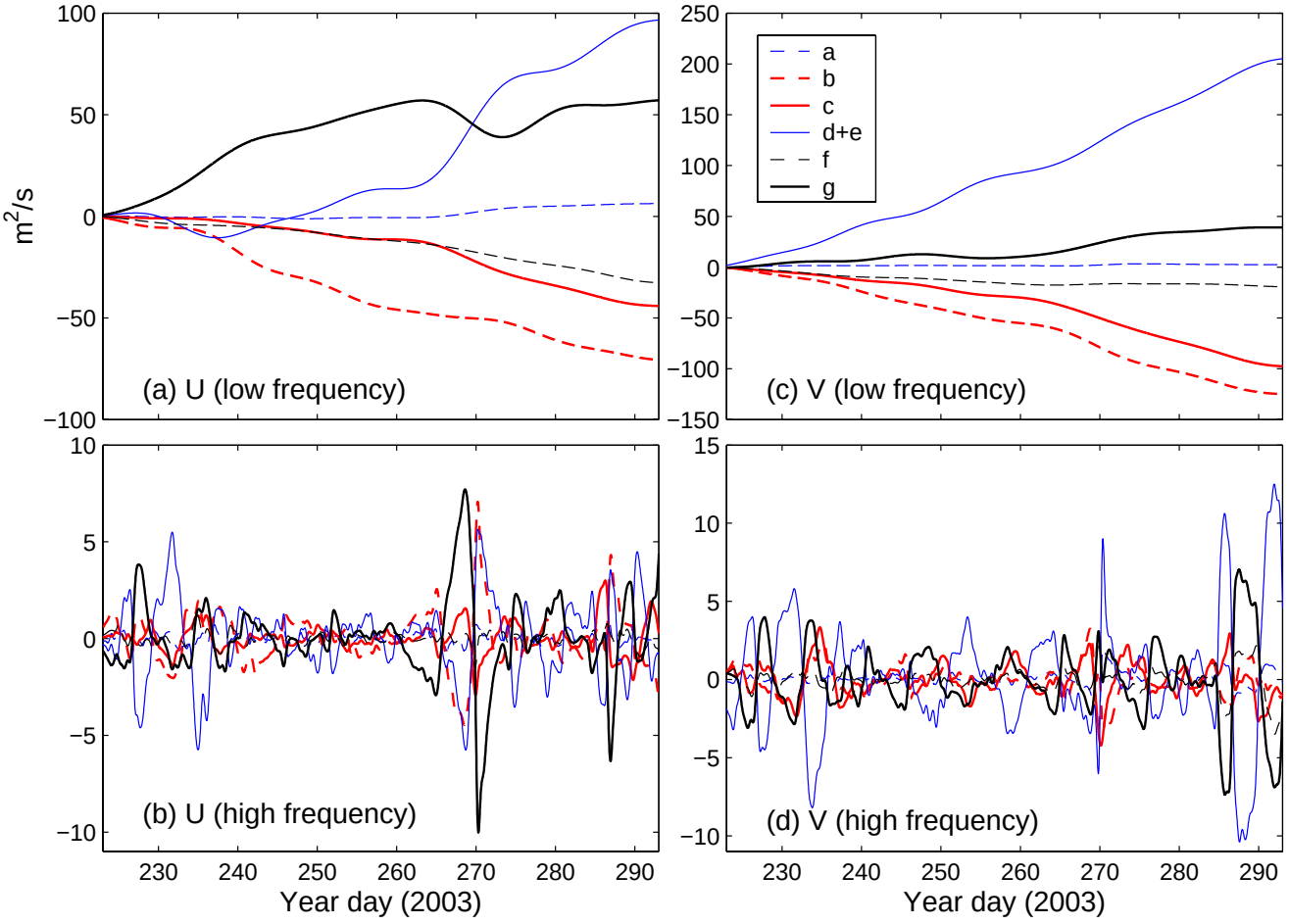

Figure 16. Time series of (a) low-frequency and (b) high-frequency momentum balances in the east direction, and (c) low-frequency and (d) high-frequency in the northward direction. The local acceleration term is indicated by the dashed blue line, the advection term by the dashed red line, the Coriolis term by the red line, the pressure gradient term by the blue line, the horizontal mixing term by the dashed black line, and the difference between surface wind stress and bottom friction by the black line.